



Conversion of CO₂ to defective porous carbons in one electro-redox cycle for boosting electrocatalytic H₂O₂ production

Ao Yu^a, Guoming Ma^a, Longtao Zhu^a, Ruiling Zhang^a, Yaozhou Li^a, Shaoting Yang^a, Hsien-Yi Hsu^b, Ping Peng^{a,*}, Fang-Fang Li^{a,*}

^a State Key Laboratory of Materials Processing and Die & Mould Technology, School of Materials Science and Engineering, Huazhong University of Science and Technology, 1037 Luoyu Road, Wuhan 430074, PR China

^b School of Energy and Environment & Department of Materials Science and Engineering, City University of Hong Kong, Kowloon Tong, Hong Kong, PR China



ARTICLE INFO

Keywords:

Carbon dioxide conversion
Defective carbon
Electrochemical redox
Molten salt
Hydrogen peroxide

ABSTRACT

Conversion of CO₂ to catalytically active carbons for electrochemical synthesis of hydroxide peroxide (H₂O₂) is highly desirable to replace the energy-intensive anthraquinone process, and achieve carbon utilization and emission reduction. Here, we develop an electrochemical reduction-reoxidation strategy in the in-situ conversion of absorbed CO₂ to defective porous carbons (DPCs) for boosting H₂O₂ production. By rationally varying oxidation conditions, hole and edge defects were controllably created on CO₂-derived carbons. Moreover, the defects dramatically enhanced the activity and selectivity toward the 2e⁻ oxygen reduction reaction (ORR). DPC0.5–5 obtained by electro-oxidizing the CO₂-derived carbon has edge and hole defects, delivering the H₂O₂ selectivity greater than 90%. By means of density functional theory calculations, the essential role of defects is demonstrated, and the types of defects with high activity are identified. The approach presented here not only sheds light on the value-added utilization of CO₂, but also develops the defect engineering of carbon materials.

1. Introduction

Global carbon dioxide (CO₂) emissions have increased at a concentration of ~2 ppm per year mainly due to the fossil fuel combustion and energy-intensive industrial processes, and have reached 413.3 ppm in September 2021 [1], much higher than the pre-industrial 280 ppm [2]. Development of technologies for CO₂ capture, storage, and utilization is a critical tactic to achieve the carbon neutrality goal. Although CO₂ is an unwelcome greenhouse gas, it is the main source of nature's carbon cycle and a particularly attractive carbon feedstock to highly valuable products [3–9], hydrocarbons [10–12], and carbonaceous fuels [13–16] because of its abundance and economic benefits. Efficient conversion of CO₂ into functional materials for renewable energy and electro-catalysis is a promising option to tackle the greenhouse gas effect. However, the conversion of CO₂ is still confronted with many challenges owing to the robust feature of CO₂. CO₂ is a typical molecule with a three-center delocalized π -bond structure, that is, CO₂ has certain characteristics of a triple bond. The C=O bond energy of 803 kJ/mol in CO₂ is higher than the general C=O double bond [17,18], thus its chemical properties are very stable, and highly efficient catalysts are usually required to boost its

reaction kinetics. It is fortunate that the conversion of CO₂ in molten salts can effectively promote the slow kinetics of CO₂ reactions, due to the high ionic conductivity of molten salts, high-temperature reaction environment and high solubility of CO₂ in molten salts [6]. Moreover, the heat and electricity to drive the electrolytic CO₂ splitting in molten salts can be provided by the solar-thermal system to restrain fossil fuel consumption, as described in our previous works [19–21].

On the other hand, the replacement of high carbon footprint industrial processes is another route to reduce CO₂ emissions, for example, the process of hydrogen peroxide (H₂O₂) production-H₂O₂ is an oxidant with far-flung employment including chemical synthesis, medical disinfection and degradation of sewage [22], which results in highly global demand for H₂O₂. The commercial production of H₂O₂ in 2015 is 5.5 million tons [23], and it will reach 6 million tons in 2024 [24]. H₂O₂ is currently produced by the anthraquinone oxidation process, which is unfortunately an energy-intensive process. Electrochemical synthesis of H₂O₂ with the aid of carbon-based catalysts is expected to be a promising method to replace the anthraquinone oxidation process and reduce energy-related carbon emissions.

Carbon catalysts have the advantages of good conductivity and

* Corresponding authors.

E-mail addresses: ppeng@hust.edu.cn (P. Peng), ffli@hust.edu.cn (F.-F. Li).

excellent acid/alkaline endurance [25–35]. Nevertheless, the electrocatalytic performance of pure carbons is far behind that of precious metals [36]. Introduction of defects has been acknowledged to enhance the catalytic performance [37–40]. Therefore, it is appealing to use CO₂ as the carbon feedstock to defective carbon catalysts, which can realize both the reduction in carbon footprint and the performance enhancement of catalytic carbon materials. However, controllable construction of defects on carbonate electrolysis carbons is rarely achieved. In addition, the current CO₂ conversion pathway has been limited to reduction methods.

Herein, we develop a low-carbon-footprint electrochemical reduction-reoxidation process, in which CO₂ captured by molten carbonate is firstly electrochemically deposited as carbon on the cathode, then the carbon-coated cathode is reversed as the anode for electrochemically oxidizing the deposited carbon to defective porous carbons (DPCs) with holes and edges. The defects can be controlled by the reoxidation time (ROT) and current. The catalytic activities of these defective carbons are evaluated by a two-electron oxygen reduction reaction (2e⁻ ORR) to H₂O₂. The as-obtained DPC0.5–5 carbon catalyst exhibits enhanced performance of 2e⁻ ORR in 0.1 M KOH solution, delivering the H₂O₂ selectivity surpassing 90% over a potential range of 0.35–0.7 V_{RHE}, and approaching 100% at 0.75 V_{RHE}. DFT calculations are performed to identify defect active sites. The electro-redox strategy presents a simple approach for preparing defective carbons with catalytic performances, as well as provides a new avenue for high-value usage of CO₂.

2. Experimental section

2.1. Materials

Industrial grade Li₂CO₃ (99 wt%) is purchased from Shanghai China Lithium Industrial Co., Ltd. Li₂CO₃ (AR) and Na₂CO₃ (AR) are purchased from China National Pharmaceutical Group Corporation. Nickel wire and galvanized steel are purchased from Alibaba and Amazon. Unless otherwise noted, all chemicals are used without further purification.

2.2. Characterizations

SEM images are obtained on FEI nova 650 and Vega 30, TEM is carried out in Tecnai Tolars FX200 with an acceleration voltage of 200 kV. X-ray diffraction patterns (tested with SHIMADZU XRD-7000) and Raman spectra (tested with LabRAM HR800) are obtained to determine the structures and compositions of the samples. XPS curves are tested by Thermo ESCALAB 250XI to confirm the content and chemical state of carbon and oxygen elements.

The calibration of collection efficiency was conducted in 0.01 M K₃Fe(CN)₆ + 0.1 M KCl aqueous solution. The working electrode, counter electrode and reference electrode were RRDE, graphite rod and SCE, respectively. The linear polarization curves were tested in the range of –0.5–0.5 V (vs. SCE) (Fig. S1). The ring voltage was set at 0.4 V (vs. SCE). The collecting coefficient N = I_{Ring}/I_{Disc}.

2.3. Synthesis of DPCs

The Nickel wire (d = 0.2 mm, 5 cm²) is bent into an “M” shaped anode. Galvanized steel (V2568, 18Ga, d = 1 mm, 5 cm²) is bent into a spring-shaped cathode. Ternary carbonate salt with a mass ratio of m(Li₂CO₃): m(Na₂CO₃): m(K₂CO₃) = 61: 22: 17 is melted at the temperature of 580 °C, then the electrodes are immersed into molten salt to start electrolysis at 4 A (800 mA cm⁻²) current for half an hour, which resulted in the reduction of CO₂ into carbons. Then the carbon-coated cathode is reversed as the anode to oxidize the deposited carbons at 0.5 A (100 mA cm⁻²) for 3, 5, 7 and 11 min, respectively to obtain the defective porous carbons (DPCs). The electrolysis was conducted in open air. After the electrolysis, the products were immersed into 6 M HCl

overnight to accelerate the dissolution of carbonates or other metallic compounds, then washed with DI water and separated by filtration. The products were collected and placed into a vacuum oven at 80 °C overnight to remove moisture. The current efficiency (η) for the reduction of tetravalent carbon (CO₃²⁻/CO₂(absorbed)) to zero-valent carbon is calculated based on Eq. 1.

$$\eta = \frac{m}{i \times t \times \frac{M_C}{F \times 4}} \times 100\% \quad (1)$$

where i is the electrolysis current, t is the electrolysis time for CO₃²⁻/CO₂(absorbed) reduction, m is the mass of the deposited carbon, F (98485 C mol⁻¹) is the Faraday's constant, M_C (12 g mol⁻¹) is the molar mass of carbon. t (1800 s) is the electrolysis time for CO₃²⁻/CO₂(absorbed) reduction (Fig. S2). When 4 A (800 mA cm⁻²) was applied for 30 min during the carbon deposition process, the mass of the deposited carbon is 221.6 mg. The current efficiency (determined by comparing the moles of applied charge to the moles of the obtained carbon) is calculated to be 99% according to Eq. 1. Based on the Eq. 2, when 7200 C electricity is applied to the electrolysis, 812.6 mg CO₂ needs to be reduced if 221.6 mg of carbon product is directly and exclusively from gaseous CO₂.

$$m(\text{CO}_2) = m(\text{C}) \times \frac{M_{\text{CO}_2}}{M_C} \quad (2)$$

where the $m(\text{CO}_2)$ and $m(\text{C})$ represent the mass of reduced CO₂ and the deposited carbon, respectively. M_{CO_2} (44 g mol⁻¹) is the molar mass of CO₂, M_C (12 g mol⁻¹) is the molar mass of carbon.

Taking the synthesis of DPC0.5–5 as an example, the electricity consumed for (Ec) carbon materials is 37.05 kWh Kg⁻¹ calculated based on Eq. 3.

$$Ec = \frac{i_1 \int_0^{t_1} V_1 dt_1 + i_2 \int_0^{t_2} V_2 dt_2}{m(\text{DPC})} \quad (3)$$

where i_1 (4 A) is the electrolysis current for CO₃²⁻/CO₂(absorbed) reduction (Fig. S2a), i_2 (0.5 A) is the electrolysis current for carbon oxidation (Fig. S2b). V_1 and V_2 are the electrolysis voltages (Fig. S2). t_1 is the electrolysis time for CO₃²⁻/CO₂(absorbed) reduction and t_2 is the electrolysis time for carbon oxidation (Fig. S2). Ec represents the consumed electricity and m (DPC) (217.1 mg) is the obtained defective carbon materials.

The current efficiency of the anodic process (η) is calculated to be 96.49% according to the Eq. 4.

$$\eta = \frac{\Delta m}{i \times t \times \frac{M_C}{F \times 4}} \times 100 \quad (4)$$

where the Δm (4.5 mg) represents the mass discrepancy of the deposited carbon and the defective carbon after anodic process, i (0.5 A) is electrolysis current for carbon oxidation, t (300 s) is the electrolysis time for carbon oxidation, F (98485 C mol⁻¹) is the Faraday's constant, M_C (12 g mol⁻¹) is the molar mass of carbon.

2.4. Electrochemical tests for H₂O₂ production

The DPC samples are dispersed in isopropanol to achieve a catalyst concentration of 5 mg ml⁻¹ with 5 wt% Nafion. After sonication for 80 min, 6 μ l ink is dropped on the RRDE (Rotating Ring Disk Electrode) (area: 0.126 cm²). The electrochemical tests are performed with CHI 760E. In the three-electrode system, 0.1 M KOH is used as the electrolyte; RRDE, graphite rod and saturated calomel electrode are used as a working electrode, a counter electrode, and a reference electrode, respectively. All the tests were conducted at room temperature. To calculate the selectivity of H₂O₂, the rotating ring-disk electrode is used to quantify the amount of H₂O₂, which is potentiostat at 1.5 V (versus the reversible hydrogen electrode) to ensure HO₂⁻ oxidation in O₂

saturated 0.1 M KOH·H₂O₂ selectivity of DPCs on the rotating ring-disk electrode is calculated based on the Eq. 5:

$$\% \text{H}_2\text{O}_2 = 100 \times \frac{2I_R/N}{I_D + I_R/N} \quad (5)$$

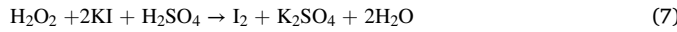
The number of electrons transferred (n) is calculated based on Eq. 6:

$$n = \frac{4I_D}{I_D + I_R/N} \quad (6)$$

where I_R is the ring current, I_D is the disk current and N is the measured collection efficiency (N = 0.43).

2.5. Iodometric titration

The DPC0.5–5 are dispersed in isopropanol to achieve a catalyst concentration of 5 mg ml⁻¹ with 5 wt% Nafion. After sonication for 80 min, 180 µl ink is dropped on the carbon cloth (area: 1.5 cm²) to form a catalytic electrode with a mass loading of 0.6 mg cm⁻². The electrochemical tests are performed with CHI 760E workstation. O₂-saturated 0.1 M KOH (80 ml) is used as the electrolyte; catalyst loaded carbon cloth, graphite rod and saturated calomel electrode are used as a working electrode, a counter electrode, and a reference electrode, respectively (Fig. 4g). The electrolysis was conducted with a constant voltage of 0.5 V_{RHE} for 1 h, 2 h and 3 h, respectively. Then 5 ml of electrolyte containing hydrogen peroxide was sucked up with a pipette and dropped into a solution containing 5 ml 3.5 M H₂SO₄, 5 ml 2 wt% KI and 250 µl molybdate catalyst (1 g ammonia molybdate dissolved in 10 ml 6 M ammonia water), which is denoted as solution A. Subsequently, 1 ml 1 wt% Starch aqueous solution was added into solution A to form a dark blue solution (denoted as solution B). The color change is attributed to the formation of pure I₂ (Eq. 7). Finally, 5 mM Na₂S₂O₃ was dropped into solution B until dark blue disappeared (Eq. 8) and the consumed volume was recorded for further use. Faraday efficiency is calculated according to Eq. 9.



$$\text{Faraday efficiency (\%)} = \frac{16\text{Vc} \times 96485}{\text{Q}} \times 100\% \quad (9)$$

Where the V, c and Q represent the consumed volume of Na₂S₂O₃, the concentration of Na₂S₂O₃ and the applied charge during the electrolysis, respectively.

2.6. DFT computational details

Density functional theory (DFT) as carried out in the Vienna Ab-initio Simulation Package (VASP) was performed to optimize geometry structures [41,42]. The exchange-correlation interactions were described by the generalized gradient approximation (GGA) [43] in the form of the Perdew-Burke-Ernzerhof functional (PBE) [44]. A cut-off energy of 500 eV for plain-weave basis sets was adopted and the convergence threshold was 10⁻⁵ eV, and 5 × 10³ eV/Å for energy and force, respectively. DFT+D3 method using empirical correction in Grimme's scheme was used to describe the weak interaction [45]. The vacuum space was set to be more than 15 Å, which was enough to avoid the interaction between periodical images. For the defective graphene model, one layer of 6 × 7 supercell was built with three different holes, and the corresponding structures are shown in Fig. 5a. For armchair and zigzag graphene, H atoms were added to saturate the dangling carbon atoms except for the active sites.

The reaction Gibbs free energy changes (ΔG) for each elementary step of 2e⁻ ORR process was based on the computational hydrogen electrode model, which can be calculated by the following Eq. 10;

$$\Delta G = \Delta E + \Delta ZPE - T\Delta S + \Delta G_U + \Delta G_{pH} \quad (10)$$

where ΔE is obtained directly from DFT calculations, ΔZPE is the change of zero-point energies (ZPE), T is the temperature of 298.15 K, and ΔS is the change in entropy of products and reactants. ΔG_U = -eU_{is} is the contribution of electrode potential to ΔG, and ΔG_{pH} = -k_BTln10 * pH.

3. Results and discussion

3.1. Synthesis and characterization of DPCs

The schematic of the electroreduction and reoxidation of CO₃²⁻/CO₂ (absorbed) to defective carbons in molten carbonate eutectic is depicted in Fig. 1. First, a constant current of 4 A is applied to reduce the CO₃²⁻/CO₂ (absorbed) to neutral carbons on the cathode in 580 °C molten Li₂CO₃-Na₂CO₃-K₂CO₃, then the deposited carbons on the cathode are oxidized under 0.5 A (100 mA cm⁻²) for 3, 5, 7 and 11 min, respectively by reversing the current direction to prepare the defective porous carbons (denoted as DPC0.5-x, x = 3, 5, 7, and 11). The detailed synthetic procedures of DPCs can be found in the Experimental Section. During the electro-deposition, CO₃²⁻ is reduced to carbon on the steel cathode (CO₃²⁻ + 4e⁻ → 3 O²⁻ + C) and oxygen on the nickel anode (3 O²⁻ → O₂ + 4e⁻). The generated O²⁻ directly absorbs the ambient CO₂ to replenish CO₃²⁻ (O²⁻ (dissolved) + CO₂ → CO₃²⁻ (molten)). The consumed carbonates were directly replaced by absorbed CO₂ [46,47], leading to the net CO₂ splitting to carbon and oxygen (CO₂ → C_(cathode) + O_(anode)) [48].

In the subsequent electrochemical reoxidation stage, the carbon-coated steel electrode is reversed as the anode, resulting in partial carbons to react with the CO₃²⁻ (C + 2CO₃²⁻ → 3CO₂ + 4e⁻) and dissolved O²⁻ (C + 2 O²⁻ → CO₂ + 4e⁻) to form defective carbons [49]. The efficiency for the anodic process is ca. 96.49% calculated based on the mass loss of the deposited carbon (Eq. 5). The CO₂ produced at the same time is in-situ captured by O²⁻ in the electrolyte (Fig. 1). The CO₂ cycle was realized by this synergistic process of electrochemical and chemical reactions, a key feature of which is to reverse the direction of current flow by simply swapping two electrodes to accomplish the etching of the deposited carbon to defective carbon.

The structural evolution of DPCs with oxidation time is shown in Fig. 2. DPC0.5–3 is a network structure composed of grafted nanosheets (Fig. 2b, f) and its carbon matrix exhibits a relatively smooth surface (Fig. 2j). As the ROT prolonged to 5, 7 and 11 min, the network structure gradually collapsed (Fig. 2c-e, g-i) and defects including holes and edges are clearly observed on the nanosheets of DPC0.5–5, DPC0.5–7 and DPC0.5–11 (Fig. 2k, l, m). In addition, QR (Quick response) code-like structures composed of a large number of highly distorted lattices with different degrees of warping were observed in DPCs (Fig. S3), reflecting the generation of bounteous intrinsic defects on carbon. The structural variation of DPCs verifies the defect-constructed effect of the oxidation process. Under the electrochemical oxidation, part of the carbon was etched, leading to the formation of hole and edge defects, which can serve as effective active sites to facilitate the 2e⁻ ORR.

To further understand the impacts of electrochemical reoxidation process on carbon structures, Brunauer-Emmett-Teller (BET) measurements were carried out. As the N₂ adsorbed curves shown in Fig. 3a, DPC0.5-x exhibit typical type-IV curves, indicating the existence of mesopores [50]. The pore volume and specific surface area (SSA) of DPC0.5-x are gradually increased with the extension of ROT (Fig. 3b-c) due to the generation of holes and edges under electrochemical oxidation, and such defects could tune the electron distribution of the carbon matrix and significantly affect the electrocatalytic activity.

X-ray Photoelectron Spectroscopy (XPS) was conducted to analyze the chemical composition of DPC0.5-x. Full survey spectra of DPC0.5-x present only the C and O elements (Fig. S4). The content of oxygen is about 10% (Table S1), introduced mainly in the form of C-O and C=O

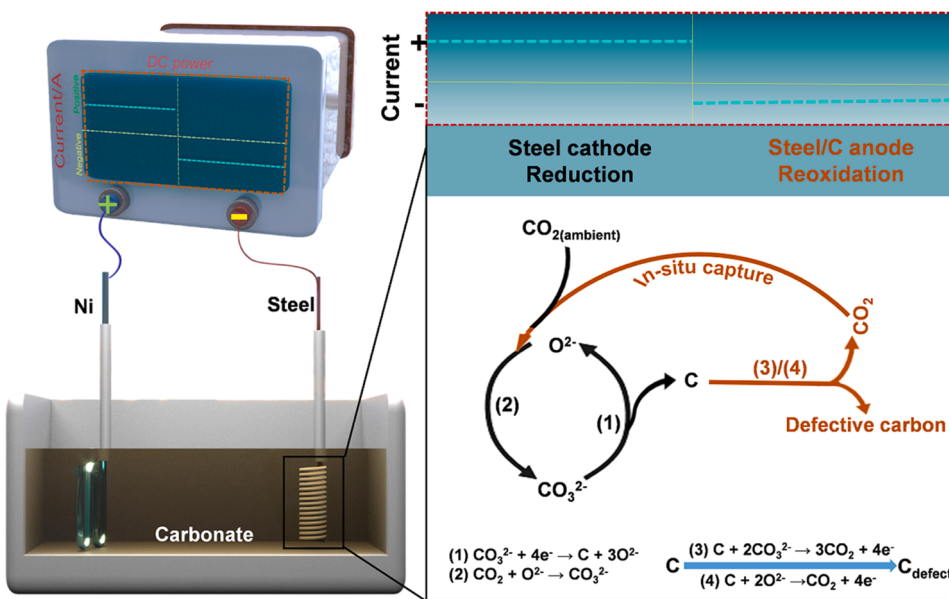


Fig. 1. Schematic illustration of the synthesis of DPCs by electrochemical reduction-reoxidation of CO_2 in molten salts.

functional groups (Fig. S5), and the C-O is dominated by ether, epoxide and edge -O- as depicted in the infrared spectra (Fig. S6). It is worth noting that the oxygen content (Table S1) and the ratio of C-O to C=O (Table S2) are nearly equal in DPC0.5-x samples, thus the influence of oxygen functional groups on our ORR measurement can be excluded, which means only defects affect most to the ORR performance. Furthermore, the catalytic activity of oxygen functional groups towards the 2e^- ORR has been well established [51,52]. Therefore, we only focus on the impact of defects on the 2e^- ORR performance in the following discussion. sp^3 carbon ($\text{sp}^3\text{-C}$, 285.4 eV) and sp^2 carbon ($\text{sp}^2\text{-C}$, 284.5 eV) associated with the defected and non-defected carbons, respectively were divided from the C1s high resolution spectra of DPC0.5-x (Fig. 3d) [53,54]. The presence of $\text{sp}^3\text{-C}$ configuration indicated the intrinsic defects on carbon surface [55]. Moreover, the content of $\text{sp}^3\text{-C}$ and the ratios of $\text{sp}^3\text{-C}/\text{sp}^2\text{-C}$ increased significantly with the extension of ROT (Fig. 3d and Fig. S7), suggesting that the defects are gradually increased. To exhibit a more intuitive representation of the defects in DPCs, Raman curves are plotted in Fig. 3e. All the DPC0.5-x display typically D band (centered at 1360 cm^{-1}) and G band (centered at 1580 cm^{-1}), referring to the disordered $\text{sp}^3\text{-C}$ structural defects and the ordered graphitic in-plane vibration of the $\text{sp}^2\text{-C}$, respectively. The increased I_D/I_G values of DPC0.5-x manifest the enhanced defective density with oxidation time (Fig. 3f). The species of defects are analyzed by examining the vibration mode of the D bands using Gaussian numerical simulation (Table S3). As shown in Fig. 3e, due to the prolonged oxidation time, the D1 band representing the exposed edge defect on the graphene layers is significantly enhanced, resulting in the enlarged area ratio of D1 to G' band (marked with $I_{D1}/I_{G'}$, an index to assess the defective degree of carbons) (Fig. 3f). The variation trend of $I_{D1}/I_{G'}$ is highly in line with that of I_D/I_G . Thus, rational control of defect density was realized by varying the oxidation time, thereby making up for the shortcomings of producing "random" defects in most synthetic methods. X-ray diffraction (XRD) results of DPC0.5-x exhibit typical graphite peaks of (002) plane (located at about 22°) and (101) plane (located at about 43°) (Fig. S8). With the gradual extension of ROT, the (002) plane of DPCs shifted to a higher angle, implying that the carbon layers are squeezed and the lattices deformation is intensified, which resulted in the generation of sufficient carbon defects.

3.2. Electrochemical 2e^- ORR measurements

The structural characteristics of DPCs reveal that they are promising ORR catalysts. The catalytic effects of DPC0.5-x on O_2 were first demonstrated by cyclic voltammetry (CV), showing significant reduction peaks in O_2 -saturated 0.1 M KOH. (Fig. S9). The electrochemical double layer capacitance (C_{dl}) reflecting the ORR activity (including 2e^- ORR and 4e^- ORR) was derived from the cyclic voltammetry curves (Fig. S10). The C_{dl} values of DPC0.5-3 and DPC0.5-5 are 18.1 and 17.82 mF/cm^2 , which is between DPC0.5-7 (21.25 mF/cm^2) and DPC0.5-11 (12.39 mF/cm^2). Electrochemical impedance spectroscopy (EIS) was measured to survey the state of charge transfer of defective DPC0.5-x samples. The semicircle of DPC0.5-5 is slightly larger than that of DPC0.5-3, while the semicircle of DPC0.5-7 is smaller. DPC0.5-11 had the largest semicircle (Fig. S11a), indicating the high charge transfer resistance (R_{ct}) and the adverse effect of high defect levels on effective charge transfer. EIS results are highly consistent with the ORR activity trend. Furthermore, the DPC0.5-5 shows the smallest Tafel slope value of 52.33 mV dec^{-1} compared to DPC0.5-3 (66.19 mV dec^{-1}), DPC0.5-7 (55.17 mV dec^{-1}) and DPC0.5-11 (55.84 mV dec^{-1}), manifesting the fastest kinetic process among the four samples (Fig. S11b-c). Thus, the defect density on carbon catalysts should be created in a controllable way.

The 2e^- ORR properties of the catalysts are further evaluated by linear scan voltammetry (LSV) (Fig. 4a). DPC0.5-5 shows the highest onset potential of $0.75\text{ V}_{\text{RHE}}$ among four DPC samples (Fig. 4a), which is approaching the thermodynamic limit of 2e^- ORR. [24] Although the disc current (corresponding to 4e^- ORR and 2e^- ORR process) of DPC0.5-5 is smaller than that of DPC0.5-3, the ring current (corresponding to 2e^- ORR process) of DPC0.5-5 is significantly higher, which suggests the contribution of increased defects in DPC0.5-5 to the 2e^- ORR. Unexpectedly, when the ROT is prolonged to 7 min, the disk current of DPC0.5-7 increased significantly, while the ring current decreased slightly compared to DPC0.5-5, which illustrates the contribution of the increased defects in DPC0.5-7 to the 4e^- ORR. Further extending ROT to 11 min, both the disk and ring currents of DPC0.5-11 reduced remarkably, which is attributed to the charge transfer obstruction caused by the severe destruction of the carbon structure. Higher ring current densities of DPC0.5-5 at selected voltages reveal its appealing activity towards H_2O_2 production (Fig. 4b). Moreover, DPC0.5-5 exhibits the H_2O_2 selectivity over 90% within $0.35\text{--}0.75\text{ V}_{\text{RHE}}$

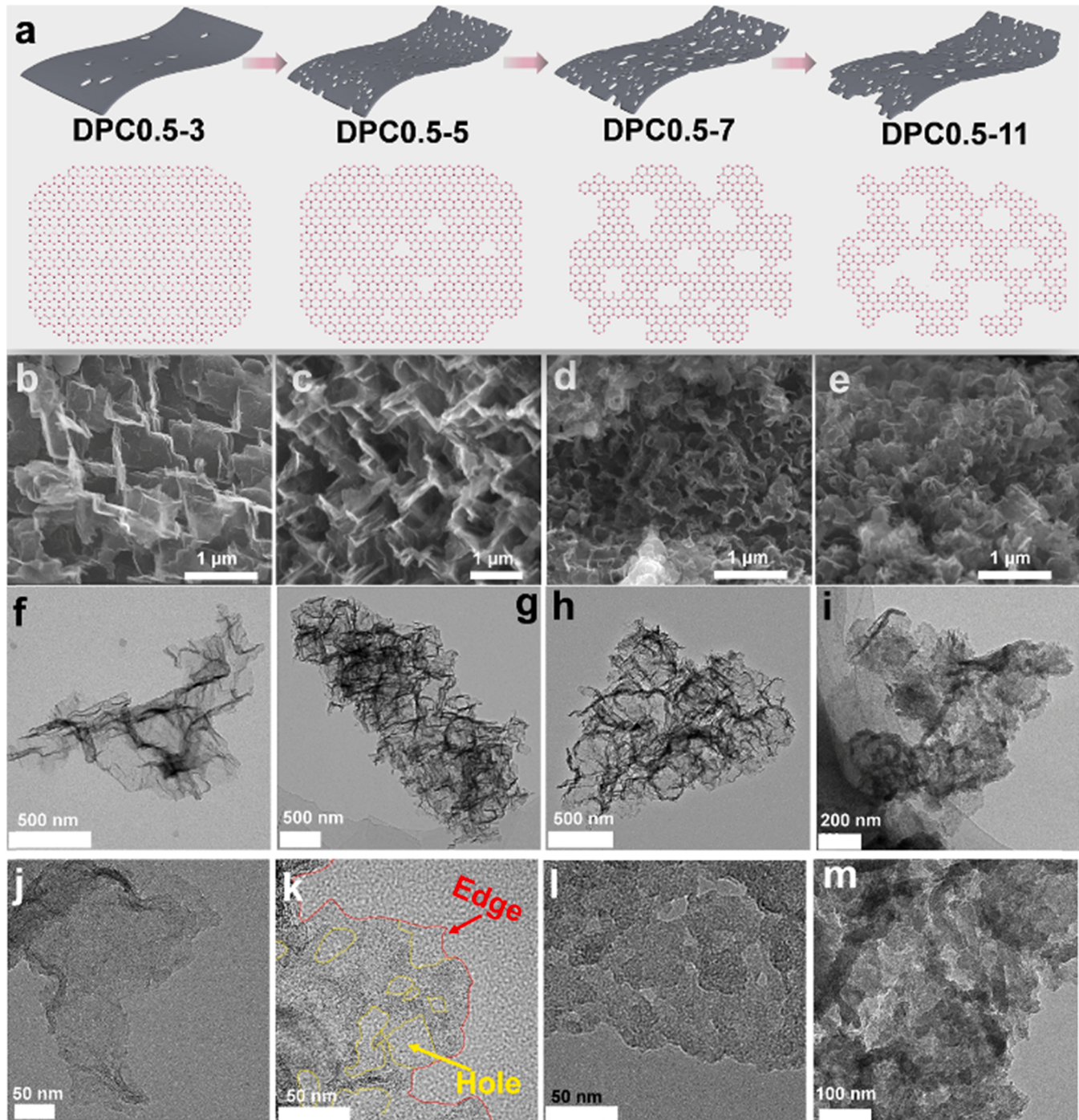


Fig. 2. (a) Schematic of the structures of DPC0.5-x at different ROT. SEM images of (b) DPC0.5-3, (c) DPC0.5-5, (d) DPC0.5-7 and (e) DPC0.5-11. TEM images of (f, j) DPC0.5-3, (g, k) DPC0.5-5, (h, l) DPC0.5-7 and (i, m) DPC0.5-11.

with an electron transfer number of ~ 2 (Fig. 4c), which is superior to that of oxygen-deficient carbon nanotube ($\sim 60\%$) [53], commercial mesoporous carbon (CMK) ($\sim 50\text{--}55\%$) [56], Pt/TiN ($\sim 65\text{--}68\%$) [57], Co-NG(O/R) (80%) [58], oxidized HPMO-filled SWCNTs ($\sim 80\%$) [59], and the N-doped graphene ($\sim 82\%$) [34] (Fig. 4d). DPC0.5-5 also displays excellent long-term durability, as manifested by the $i-t$ curve showing no fading of ring current density over 12 h (Fig. 4e), which elucidates that the defects can withstand long-term electrocatalytic reactions. In contrast, the unoxidized deposited carbon (DPC) has a low H_2O_2 selectivity of 60% compared to that of DPC0.5-x (Fig. S12c), which manifested the crucial reoxidation effect on the promotion of 2e^- ORR.

The CV curves, LSV curves and electron transfer numbers of DPC can be achieved in Fig. S12. HRTEM image of DPC in Fig. S11e shows that there are no obvious hole and edge defects on the carbon matrix. The high I_D/I_G value of DPC (Fig. S12f) is mainly attributed to the defects from high oxygen content. The reoxidation process primarily contributed to the formation of hole and edge defects.

The relationship between H_2O_2 selectivity and defects is represented in Fig. 4f, showing the selectivity climbs first and then descends with the defective degree. The performance of 2e^- ORR and the defect density of DPC0.5-x do not conform to a linear relationship. In a sense, the increase of defects is conducive to the 2e^- ORR, but too many defects are the

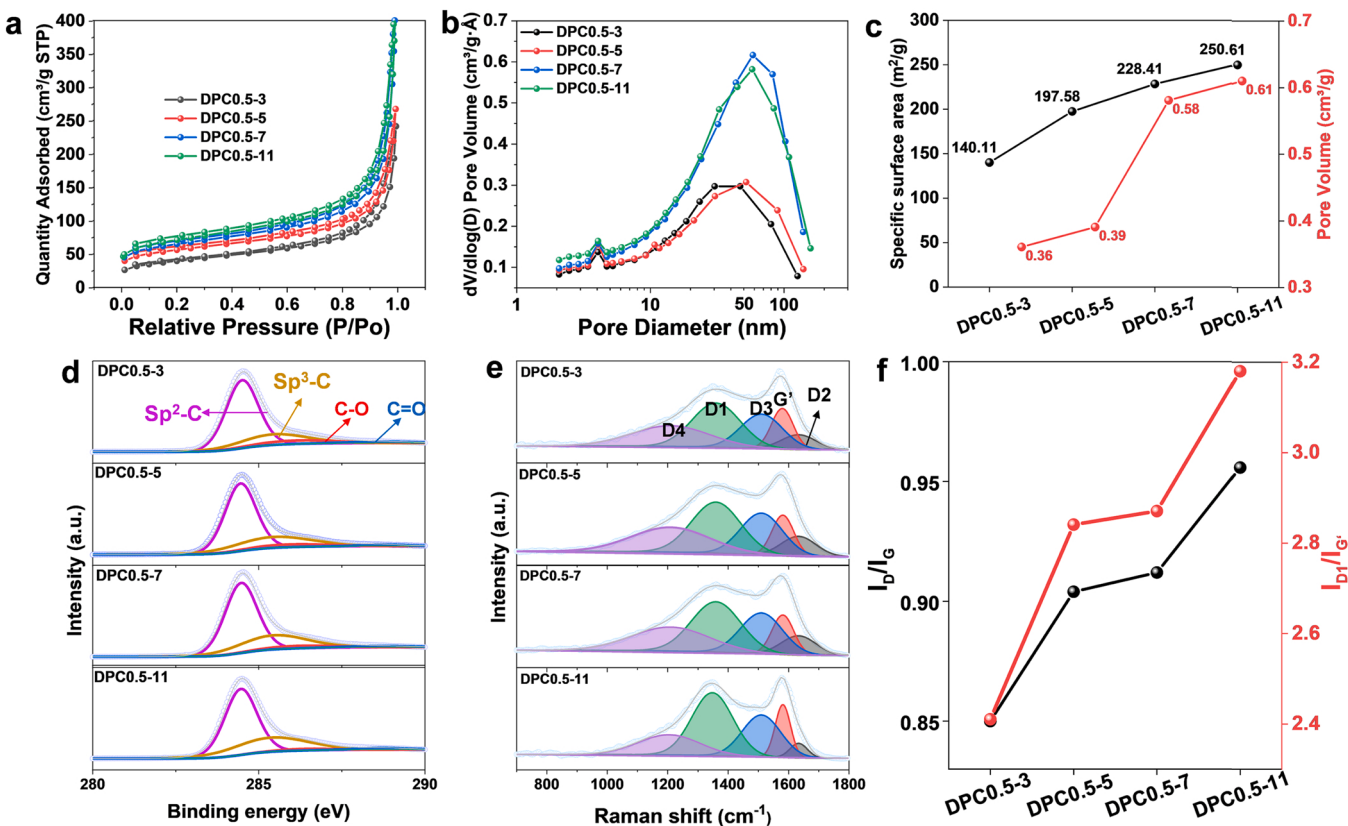


Fig. 3. (a) Nitrogen adsorption and desorption isotherm. (b) Pore width distributions. (c) calculated specific surface area and pore volume of DPC0.5-x based on BJH method. (d) C1s high resolution spectra and (e) Raman results of DPC0.5-x. (f) I_D/I_G and I_{D1}/I_G values of DPC0.5-x.

opposite, showing the significance of defect density control during the preparation process. The comparison of four defective carbons indicates the superiority of DPC0.5-5 configuration to the other three in terms of $2e^-$ ORR in 0.1 M KOH. The better performance of DPC0.5-5 was also manifested by the high H_2O_2 production rate. As shown in Fig. 4g-i, the production rate reached $115.32 \text{ mmol (g}_{cat\text{.h}})^{-1}$ at 0.5 V_{RHE}, and the faraday efficiency (FE) reached 89.0%. The results corroborate that the in-situ electrochemically constructed DPC0.5-5 is a promising $2e^-$ ORR catalyst in alkaline media.

To delve into the control of defects by electrolysis conditions, and the impact of defective degree on H_2O_2 activity and selectivity, the other two DPCs (DPC_y-5, $y = 1$ and 2) were synthesized by reoxidizing the deposited carbon at 1 A (200 mA cm^{-2}) and 2 A (400 mA cm^{-2}) instead of 0.5 A (100 mA cm^{-2}) for 5 min. When the applied current increased from 0.5 A (100 mA cm^{-2}) to 1 A (200 mA cm^{-2}) and 2 A (400 mA cm^{-2}), more defects were created, as displayed by the XRD and Raman results (Fig. S13a-b). TEM images of DPC1-5 and DPC2-5 given in Fig. S12c-d display the damaged carbon structures. The CV, LSV, H_2O_2 selectivity and charge transfer numbers of DPC1-5 and DPC2-5 are also examined as shown in Fig. S14. The H_2O_2 selectivity is decayed compared to that of DPC0.5-5, confirming that the number of defects needs to be governed, rather than the more the better. The enhancement of defect density within a certain range is beneficial to the H_2O_2 selectivity, whereas too many defects will lead to negative effects (Fig. S15).

3.3. DFT calculations

As demonstrated by the experimental results, with the extension of ROT, more defects were created in DPCs. These defects significantly contributed to the H_2O_2 production by tailoring the electronic structures of the carbon matrix, and affected the charge transfer between the active sites and reacting matters. Density functional theory calculations (DFT)

were performed to clarify the catalytic activity of defect sites on H_2O_2 formation. The formation of defects on the carbon matrix originated from the destruction of six-membered ring structures of graphene layers and the hole and edge defects are located on the stacked graphene layers. According to the Raman curves (Fig. 3e), D1 (graphene layer edges) and D2 (surface graphene layer) bands representing the exposed defects on the edge and surface of graphene layers are dominant in the samples. XRD patterns of DPC0.5-x ($x = 3, 5, 7, 11$) exhibit typical graphitic features (Fig. S8). Furthermore, HR-TEM images of DPC0.5-x as shown in Fig. S16 display plenty of distorted lattice fringes, indicating graphitic carbon configurations. Thus, the DFT calculations were based on graphene defect structures. Five geometrically optimized defective models are built and schematically illustrated in Fig. 5a, including zigzag and armchair edges, hole 1, hole 2 and hole 3 on the carbon matrix. The adsorption energies of O_2 binding with different defect sites in the most stable configurations are calculated and summarized in Fig. S17. The initial O_2 adsorption can readily occur at the zigzag and hole 2 sites given the low adsorption energies (Fig. S17f). Due to the low energy barriers of zigzag and hole 2 sites, the O_2 molecules could be easily activated to generate the pivotal intermediate OOH species.

The charge states of the five models are also calculated to clarify the electronic structure and the different adsorption energies of O_2 . As shown in Fig. 5b, the charge states of the defect-related carbon atoms (bonded with hydrogen atoms) in zigzag and hole 2 are more negative due to the accumulation of electrons, making these carbon atoms easier to absorb O_2 , resulting in lower O_2 adsorption energy. Whereas in the case of armchair, hole 1 and hole 2, the charge states are more positive, leading to higher O_2 adsorption energy.

For the $2e^-$ ORR, the absorption of the O_2 was followed by the protonation of O_2 to OOH^* (Eq. 11) and OOH^* reduction to H_2O_2 (Eq. 12). While the competitive $4e^-$ ORR triggers a diverse reaction pathway

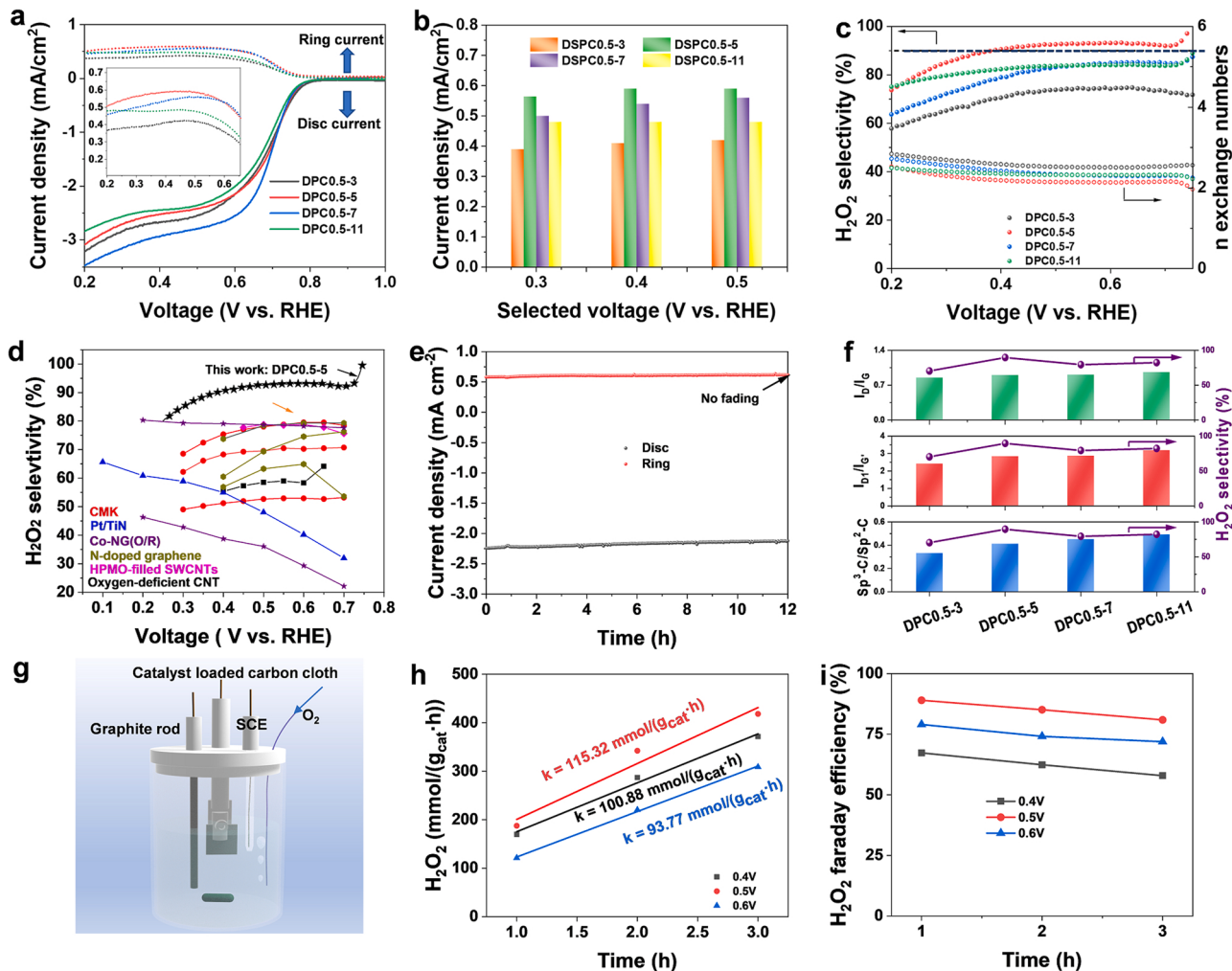
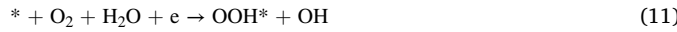


Fig. 4. (a) Polarization curves of DPC0.5-x at 1600 rpm (solid lines) and simultaneous H_2O_2 detection currents at the ring electrode (dashed lines) for the DPC0.5-x. (b) Ring current density of DPC0.5-x at different voltages. (c) Calculated H_2O_2 selectivity and the corresponding electron transfer numbers of DPC0.5-x at various potentials. (d) Comparison with some previous works. (e) Stability test of DPC0.5-5 at a selected voltage of 0.5 V_{RHE} . (f) The variation trend of average H_2O_2 selectivity with $I_{\text{D}}/I_{\text{G}}$, $I_{\text{D}1}/I_{\text{G}}$, and $\text{Sp}^3\text{-C}/\text{Sp}^2\text{-C}$. (g) Scheme of the full cell setup for H_2O_2 production. (h) H_2O_2 production normalized to catalyst loading over the reaction time. (i) H_2O_2 faradaic efficiency (%) tested at different applied potentials with the catalyst loading of 0.6 mg cm^{-2} . All the experiments were conducted in 0.1 M KOH.

where H_2O is generated (Eq. 13).



in which * denotes an unoccupied active site, OH^* and OOH^* denote the single adsorbed intermediate for the reaction. In terms of a catalyst with high 2e^- ORR catalytic activity, optimizing the adsorption energy of OOH^* is of great significance for minimizing the thermodynamic barrier of the 2e^- pathway and maximizing the barrier of the 4e^- pathway. For the 2e^- pathway, the thermodynamic limit potential expressed in U_{L} is 0.7 eV, at which the total free energy barrier becomes zero [51,53,60,61], and the free energy of all reaction steps are decreasing. The difference between the limiting potential and equilibrium potential is defined as the theoretical overpotential. The binding energy of OOH^* to active sites is the key parameter in evaluating the catalyst selectivity [60]. Therefore, ΔG_{OOH^*} was used as a function to plot the activity volcano of different defects (Fig. 5c). The ideal catalyst, at the peak of the volcano, has a ΔG_{OOH^*} 4.22 eV and overpotential 0 V, and its free-energy diagram is flat at the equilibrium potential (Fig. 5d). The

binding energy of different active sites to OOH^* determined the limiting step. The active sites located on the right side of the volcano bind OOH^* weakly, resulting in a limiting step Eq. (3). On the contrary, those located on the left side bind OOH^* strongly, resulting in a limiting step Eq. (4) [53]. Therefore, the 2e^- ORR activity is eventually determined by the binding strength of OOH^* to the active sites. The computerized values shown in Fig. 5c-d imply that the hole 2 and zigzag defects are highly active for the 2e^- ORR to H_2O_2 , and hole 2 is the most active, yielding an overpotential of 0.05 eV (Fig. 5c). Because the adsorption energy of OOH^* is dominated by the orbital fillings of adsorption sites [62], therefore, the partial density of states (PDOS) of 2p orbitals of adsorption sites (defect sites) are calculated.

Apparently, the adsorption sites exhibit different features of electron occupations. The C-2p peaks of hole 2 and zigzag at the Fermi level are strongly enhanced, which improves the orbital overlap of OOH^* and However, C-2p peaks for hole 1 and armchair are not emerged and become a fully unfilled anti-bonding state. Such an anti-bonding state would be filled by the OOH^* adsorption, leading to the enhancement of the energy of the product state and the significant reduction of chemical adsorption. For hole 3, the intensity of the C-2p peak at the Fermi level is between hole 2/zigzag and hole 1/armchair, demonstrating the moderate adsorption of OOH^* . DFT results also confirm that the moderate

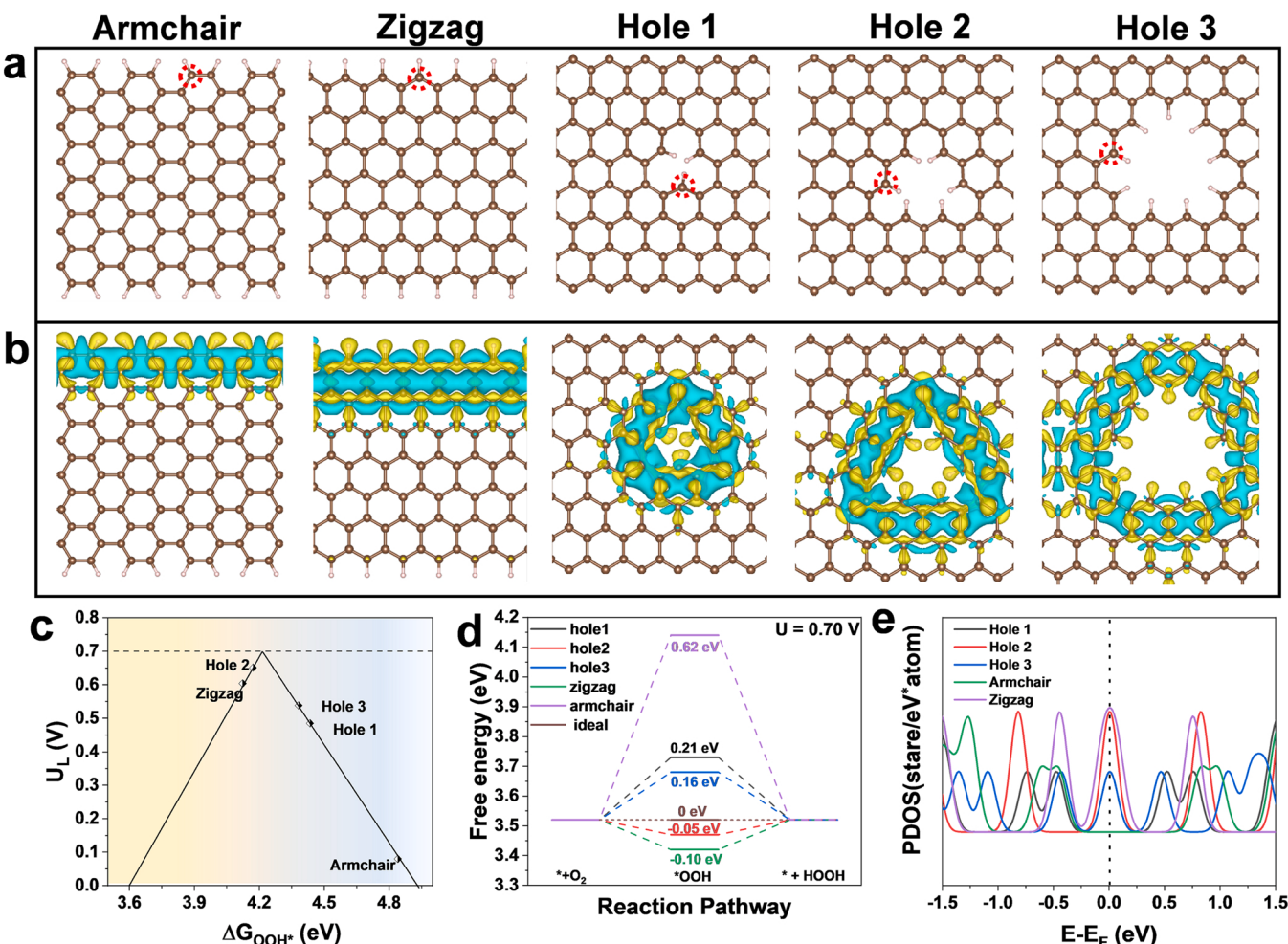


Fig. 5. DFT results of the $2e^-$ -ORR activities of different defect sites. (a) Different defect site configurations examined in this study. The carbon atoms denoted by a red circle are the active sites under investigation. (b) Charge density of armchair, zigzag, hole1, hole 2 and hole 3 defects. (c) Calculated $2e^-$ ORR-related volcano plot for the electro-reduction of O_2 to H_2O_2 displayed with the limiting potential plotted as a function of ΔG_{OOH^*} . The equilibrium potential for the $2e^-$ ORR is shown as the dashed black line. (d) Free-energy diagram of hole1, hole 2, hole 3, zigzag and armchair defects for oxygen reduction to H_2O_2 . (e) Density of states for armchair, zigzag, hole1, hole 2 and hole 3 defects carbon site and the final adsorption energy of OOH^* . (For interpretation of the references to colour in this figure, the reader is referred to the web version of this article.)

defect density is critical to catalytic activity, which is well consistent with the experimental results.

4. Conclusions

In summary, we have demonstrated herein the conversion of CO_3^{2-} / CO_2 to defective porous carbons in one electro-redox cycle. An ingenious design of this electrochemical redox process is to simply reverse the two electrodes to change the direction of electron flow, thereby oxidative etching the deposited carbons into defective carbons. Moreover, the defect density can be reasonably controlled by the reoxidation time and reoxidation current. The as-prepared DPC0.5-5 with hole and edge defects exhibits enhanced performances towards $2e^-$ ORR in terms of activity, selectivity and stability in alkaline conditions. Based on DFT calculations, the origin of the high activity is assigned to the hole 2 and zigzag edge defects. The present study not only offers a low-carbon footprint platform for controllable synthesis of defective carbon-based materials for catalysis and energy applications but also provides new insights into defect engineering on carbon materials.

CRediT authorship contribution statement

Ao Yu: Investigation, Methodology, Data analysis, Writing – original

draft. **Guoming Ma:** Methodology, Data analysis, Investigation. **Longtao Zhu:** Methodology, Data analysis. **Ruiling Zhang:** Investigation. **Yaozhou Li:** Data analysis. **Shaoting Yang:** Data analysis. **Hsien-Yi Hsu:** Data analysis. **Ping Peng:** Supervision, Conceptualization, Funding acquisition. **Fang-Fang Li:** Conceptualization, Supervision, Project administration, Funding acquisition, Writing – review & editing.

Declaration of Competing Interest

The authors declare that they have no known competing financial interests or personal relationships that could have appeared to influence the work reported in this paper.

Acknowledgements

We acknowledge the financial supports from National Natural Science Foundation of China (Grant No. 22071070, 21971077), the facility support of the Center for Nanoscale Characterization & Devices (CNCD), WNLO of HUST, and the Analytical and Testing Center in Huazhong University of Science and Technology for all related measurements.

Appendix A. Supporting information

Supplementary data associated with this article can be found in the online version at doi:10.1016/j.apcatb.2022.121161.

References

[1] [\(https://www.CO2.earth/\)](https://www.CO2.earth/).

[2] W.S. Broecker, Climate change CO₂ arithmetic, *Science* 315 (2007) 1371.

[3] P. Peng, A. Yu, J.W. Ren, F.F. Li, Electrolytic carbons from CO₂ and their applications, *ES Energy Environ.* 2 (2018) 9–20.

[4] J.W. Ren, A. Yu, P. Peng, M. Lefler, F.-F. Li, S. Licht, Recent advances in solar thermal electrochemical process (STEP) for carbon neutral products and high value nanocarbons, *Acc. Chem. Res.* 52 (2019) 3177–3187.

[5] R. Jiang, M. Gao, X. Mao, D. Wang, Advancements and potentials of molten salt CO₂ capture and electrochemical transformation (MSCC-ET) process, *Curr. Opin. Electrochem.* 17 (2019) 38–46.

[6] A. Yu, G. Ma, J. Ren, P. Peng, F.-F. Li, Sustainable carbons and fuels: recent advances of CO₂ conversion in molten salts, *ChemSusChem* 13 (2020) 6229–6245.

[7] T. Lv, J. Xiao, W. Weng, W. Xiao, Electrochemical fixation of carbon dioxide in molten salts on liquid zinc cathode to Zinc@Graphitic carbon spheres for enhanced energy storage, *Adv. Energy Mater.* 10 (2020), 2002241.

[8] X. Liang, J. Xiao, W. Weng, W. Xiao, Electrochemical reduction of carbon dioxide and iron oxide in molten salts to Fe/Fe3C modified carbon for electrocatalytic oxygen, *Evolv. Angew. Chem. Int. Ed.* 60 (2021) 2120–2124.

[9] W. Weng, B. Jiang, Z. Wang, W. Xiao, In situ electrochemical conversion of CO₂ in molten salts to advanced energy materials with reduced carbon emissions, *Sci. Adv.* 6 (2020) eaay9278.

[10] J. Shen, R. Kortlever, R. Kas, Y.Y. Birdja, O. Diaz-Morales, Y. Kwon, I. Ledezma-Yanez, K.J.P. Schouten, G. Mul, M.T.M. Koper, Electrocatalytic reduction of carbon dioxide to carbon monoxide and methane at an immobilized cobalt protoporphyrin, *Nat. Commun.* 6 (2015) 8177.

[11] W.-Y. Chu, Z. Culakova, B.T. Wang, K.I. Goldberg, Acid-assisted hydrogenation of CO₂ to methanol in a homogeneous catalytic cascade system, *ACS Catal.* 9 (2019) 9317–9326.

[12] K.M. Lee, J.H. Jang, M. Balamurugan, J.E. Kim, Y.I. Jo, K.T. Nam, Redox-neutral electrochemical conversion of CO₂ to dimethyl carbonate, *Nat. Energy* 6 (2021) 733–741.

[13] D. Ji, Y. Liu, Z. Li, D. Yuan, G. Yang, M. Jiang, Y. Wang, Y. Yu, H. Wu, A comparative study of electrodes in the direct synthesis of CH₄ from CO₂ and H₂O in molten salts, *Int. J. Hydrot. Energy* 42 (2017) 18156–18164.

[14] D. Ji, Z. Li, W. Li, D. Yuan, Y. Wang, Y. Yu, H. Wu, The optimization of electrolyte composition for CH₄ and H₂ generation via CO₂/H₂O co-electrolysis in eutectic molten salts, *Int. J. Hydrot. Energy* 44 (2019) 5082–5089.

[15] F.-F. Li, S. Liu, B. Cui, J. Lau, J. Stuart, B. Wang, S. Licht, A one-pot synthesis of hydrogen and carbon fuels from water and carbon dioxide, *Adv. Energy Mater.* 5 (2015), 1401791.

[16] F.-F. Li, J. Lau, S. Licht, Sungas instead of syngas: efficient coproduction of CO and H₂ with a single beam of sunlight, *Adv. Sci.* 2 (2015), 1500260.

[17] Y. Zheng, W. Zhang, Y. Li, J. Chen, B. Yu, J. Wang, L. Zhang, J. Zhang, Energy related CO₂ conversion and utilization: Advanced materials/nanomaterials, reaction mechanisms and technologies, *Nano Energy* 40 (2017) 512–539.

[18] M. Stanbury, J.-D. Compain, M. Trejo, P. Smith, E. Gouré, S. Chardon-Noblat, Mn-carbonyl molecular catalysts containing a redox-active phenanthroline-5,6-dione for selective electro- and photoreduction of CO₂ to CO or HCOOH, *Electrochim. Acta* 240 (2017) 288–299.

[19] S. Licht, Efficient solar-driven synthesis, carbon capture, and desalination, STEP: solar thermal electrochemical production of fuels, metals, bleach, *Adv. Mater.* 23 (2011) 5592–5612.

[20] S. Licht, B. Wang, H. Wu, STEP-A solar chemical process to end anthropogenic global warming. II: experimental results, *J. Phys. Chem. Lett.* 115 (2011) 11803–11821.

[21] S. Licht, H. Wu, STEP Iron, a chemistry of iron formation without CO₂ emission: molten carbonate solubility and electrochemistry of iron ore impurities, *J. Phys. Chem. C* 115 (2011) 25138–25147.

[22] K. Dong, Y. Lei, H. Zhao, J. Liang, P. Ding, Q. Liu, Z. Xu, S. Lu, Q. Li, X. Sun, Noble-metal-free electrocatalysts toward H₂O₂ production, *J. Mater. Chem. A* 8 (2020) 23123–23141.

[23] H. Sheng, E.D. Hermes, X. Yang, D. Ying, A.N. Janes, W. Li, J.R. Schmidt, S. Jin, Electrocatalytic production of H₂O₂ by selective oxygen reduction using earth-abundant cobalt pyrite CoS₂, *ACS Catal.* 9 (2019) 8433–8442.

[24] M. Wang, N. Zhang, Y. Feng, Z. Hu, Q. Shao, X. Huang, Partially pyrolyzed binary metal-organic framework nanosheets for efficient electrochemical hydrogen peroxide synthesis, *Angew. Chem. Int. Ed. Engl.* 59 (2020) 14373–14377.

[25] Y. Liu, X. Quan, X. Fan, H. Wang, S. Chen, High-yield electrosynthesis of hydrogen peroxide from oxygen reduction by hierarchically porous carbon, *Angew. Chem. Int. Ed. Engl.* 54 (2015) 6837–6841.

[26] S. Chen, Z. Chen, S. Siahrostami, T.R. Kim, D. Nordlund, D. Sokaras, S. Nowak, J. W.F. To, D. Higgins, R. Sinclair, J.K. Nørskov, T.F. Jaramillo, Z. Bao, Defective carbon-based materials for the electrochemical synthesis of hydrogen peroxide, *ACS Sustain. Chem. Eng.* 6 (2017) 311–317.

[27] Z. Chen, S. Chen, S. Siahrostami, P. Chakthranont, C. Hahn, D. Nordlund, S. Dimosthenis, J.K. Nørskov, Z. Bao, T.F. Jaramillo, Development of a reactor with carbon catalysts for modular-scale, low-cost electrochemical generation of H₂O₂, *React. Chem. Eng.* 2 (2017) 239–245.

[28] S. Chen, Z. Chen, S. Siahrostami, D. Higgins, D. Nordlund, D. Sokaras, T.R. Kim, Y. Liu, X. Yan, E. Nilsson, R. Sinclair, J.K. Nørskov, T.F. Jaramillo, Z. Bao, Designing boron nitride islands in carbon materials for efficient electrochemical synthesis of hydrogen peroxide, *J. Am. Chem. Soc.* 140 (2018) 7851–7859.

[29] D. Iglesias, A. Giuliani, M. Melchionna, S. Marchesan, A. Criado, L. Nasi, M. Bevilacqua, C. Tavagnacco, F. Vizza, M. Prato, P. Fornasiero, N-doped graphitized carbon nanohorns as a forefront electrocatalyst in highly selective O₂ reduction to H₂O₂, *Chem* 4 (2018) 106–123.

[30] H.W. Kim, M.B. Ross, N. Kornienko, L. Zhang, J. Guo, P. Yang, B.D. McCloskey, Efficient hydrogen peroxide generation using reduced graphene oxide-based oxygen reduction electrocatalysts, *Nat. Catal.* 1 (2018) 282–290.

[31] Y. Sun, S. Li, Z.P. Jovanov, D. Bernsmeier, H. Wang, B. Paul, X. Wang, S. Kuhl, P. Strasser, Structure, activity, and faradaic efficiency of nitrogen-doped porous carbon catalysts for direct electrochemical hydrogen peroxide production, *ChemSusChem* 11 (2018) 3388–3395.

[32] Y. Sun, I. Sinev, W. Ju, A. Bergmann, S. Dresp, S. Kühl, C. Spörli, H. Schmies, H. Wang, D. Bernsmeier, B. Paul, R. Schmack, R. Kraehnert, B. Roldan Cuena, P. Strasser, Efficient electrochemical hydrogen peroxide production from molecular oxygen on nitrogen-doped mesoporous carbon catalysts, *ACS Catal.* 8 (2018) 2844–2856.

[33] G. Chen, J. Liu, Q. Li, P. Guan, X. Yu, L. Xing, J. Zhang, R. Che, A direct H₂O₂ production based on hollow porous carbon sphere-sulfur nanocrystal composites by confinement effect as oxygen reduction electrocatalysts, *Nano Res.* 12 (2019) 2614–2622.

[34] L. Han, Y.Y. Sun, S. Li, C. Cheng, C.E. Halbig, P. Feicht, J.L. Hübner, P. Strasser, S. Egler, In-plane carbon lattice-defect regulating electrochemical oxygen reduction to hydrogen peroxide production over nitrogen-doped graphene, *ACS Catal.* 9 (2019) 1283–1288.

[35] Y. Jia, L. Zhang, L. Zhuang, H. Liu, X. Yan, X. Wang, J. Liu, J. Wang, Y. Zheng, Z. Xiao, E. Taran, J. Chen, D. Yang, Z. Zhu, S. Wang, L. Dai, X. Yao, Identification of active sites for acidic oxygen reduction on carbon catalysts with and without nitrogen doping, *Nat. Catal.* 2 (2019) 688–695.

[36] D. Xue, H. Xia, W. Yan, J. Zhang, S. Mu, Defect engineering on carbon-based catalysts for electrocatalytic CO₂ reduction, *Nano Micro Lett.* 13 (2021) 5.

[37] I.S. Amiuu, X. Liu, Z. Pu, W. Li, Q. Li, J. Zhang, H. Tang, H. Zhang, S. Mu, From 3D ZIF nanocrystals to Co-Nx/C nanorod array electrocatalysts for ORR, OER, and Zn-air batteries, *Adv. Funct. Mater.* 28 (2018), 1704638.

[38] Y. Jia, J. Chen, X. Yao, Defect electrocatalytic mechanism: concept, topological structure and perspective, *Mater. Chem. Front.* 2 (2018) 1250–1268.

[39] C. Xie, D. Yan, W. Chen, Y. Zou, R. Chen, S. Zang, Y. Wang, X. Yao, S. Wang, Insight into the design of defect electrocatalysts: From electronic structure to adsorption energy, *Mater. Today* 31 (2019) 47–68.

[40] H. Zhao, C. Sun, Z. Jin, D.-W. Wang, X. Yan, Z. Chen, G. Zhu, X. Yao, Carbon for the oxygen reduction reaction: a defect mechanism, *J. Mater. Chem. A* 3 (2015) 11736–11739.

[41] G. Kresse, J. Furthmüller, Efficient iterative schemes for ab initio total-energy calculations using a plane-wave basis set, *Phys. Rev. B* 54 (1996) 11169–11186.

[42] G. Kresse, J. Furthmüller, Efficiency of ab-initio total energy calculations for metals and semiconductors using a plane-wave basis set, *Comput. Mater. Sci.* 6 (1996) 15–50.

[43] P. J.P., B. K., E. M., Generalized gradient approximation made simple, *Phys. Rev. Lett.* 77 (1996) 3865–3868.

[44] J.P. Perdew, M. Ernzerhof, K. Burke, Rationale for mixing exact exchange with density functional approximations, *J. Chem. Phys.* 105 (1996) 9982–9985.

[45] S. Grimme, Semiempirical GGA-type density functional constructed with a long-range dispersion correction, *J. Comput. Chem.* 27 (2006) 1787–1799.

[46] B. Deng, J. Tang, X. Mao, Y. Song, H. Zhu, W. Xiao, D. Wang, Kinetic and thermodynamic characterization of enhanced carbon dioxide absorption process with lithium oxide-containing ternary molten carbonate, *Environ. Sci. Technol.* 50 (2016) 10588–10595.

[47] K. Yugo, T. Koichi, F. Satoko, F. Kenichiro, Absorption of carbon dioxide at high temperature with molten alkali carbonate using bubble column reactor, *J. Chem. Eng. Jpn.* 52 (2019) 31–40.

[48] J. Ren, F.F. Li, J. Lau, L. I.-U. S. Gonzá, Licht, One-pot synthesis of carbon nanofibers from CO₂, *Nano Lett.* 15 (2015) 6142–6148.

[49] H.V. Iijie, R.C. Lawrence, N.J. Siambun, S.M. Jeong, D.A. Jewell, D. Hu, G.Z. Chen, Electro-deposition and re-oxidation of carbon in carbonate-containing molten salts, *Faraday Discuss.* 172 (2014) 105–116.

[50] A. Yu, G. Ma, J. Jiang, Y. Hu, M. Su, W. Long, S. Gao, H.-Y. Hsu, P. Peng, F.-F. Li, Bio-inspired and eco-friendly synthesis of 3D spongy meso-microporous carbons from CO₂ for supercapacitors, *Chem. Eur. J.* 27 (2021) 10405–10412.

[51] Q. Zhang, X. Tan, N.M. Bedford, Z. Han, L. Thomsen, S. Smith, R. Amal, X. Lu, Direct insights into the role of epoxy groups on cobalt sites for acidic H₂O₂ production, *Nat. Commun.* 11 (2020) 4181.

[52] Y. Pang, K. Wang, H. Xie, Y. Sun, M.-M. Titirici, G.-L. Chai, Mesoporous carbon hollow spheres as efficient electrocatalysts for oxygen reduction to hydrogen peroxide in neutral electrolytes, *ACS Catal.* 10 (2020) 7434–7442.

[53] Z.Y. Lu, G.X. Chen, S. Siahrostami, Z.H. Chen, K. Liu, J. Xie, L. Liao, T. Wu, D. C. Lin, Y. Liu, T.F. Jaramillo, J.K. Nørskov, Y. Cui, High-efficiency oxygen reduction to hydrogen peroxide catalysed by oxidized carbon materials, *Nat. Catal.* 1 (2018) 156–162.

[54] Z. Li, X. Gillon, E. Diallo, L. Houssiau, J.J. Pireaux, A comparative study of copolymerization by r.f inductively coupled plasma, *J. Phys. Conf. Ser.* 275 (2011), 012020.

[55] Y. Cao, Z. Liu, Y. Tang, C. Huang, Z. Wang, F. Liu, Y. Wen, B. Shan, R. Chen, Vaporized-salt-induced sp₃-hybridized defects on nitrogen-doped carbon surface towards oxygen reduction reaction, *Carbon* 180 (2021) 1–9.

[56] Y.-L. Wang, S.-S. Li, X.-H. Yang, G.-Y. Xu, Z.-C. Zhu, P. Chen, S.-Q. Li, One minute from pristine carbon to an electrocatalyst for hydrogen peroxide production, *J. Mater. Chem. A* 7 (2019) 21329–21337.

[57] S. Yang, J. Kim, Y.J. Tak, A. Soon, H. Lee, Single-atom catalyst of platinum supported on titanium nitride for selective electrochemical reactions, *Angew. Chem. Int. Ed.* 55 (2016) 2058–2062.

[58] E. Jung, H. Shin, B.-H. Lee, V. Efremov, S. Lee, H.S. Lee, J. Kim, W. Hooch Antink, S. Park, K.-S. Lee, S.-P. Cho, J.S. Yoo, Y.-E. Sung, T. Hyeon, Atomic-level tuning of Co–N–C catalyst for high-performance electrochemical H₂O₂ production, *Nat. Mater.* 19 (2020) 436–442.

[59] R.T. Hu, F.F. Yao, C.X. Wu, C.H. Jin, L.H. Guan, Enhancing the production of hydrogen peroxide from electrocatalytic oxygen reduction reaction by tailoring the electronic states of single-walled carbon nanotubes: a synergistic effect from interior filling and exterior oxidation, *Sustain. Energy Fuels* 3 (2019) 1951–1956.

[60] S. Siahrostami, A. Verdaguer-Casadevall, M. Karamad, D. Deiana, P. Malacrida, B. Wickman, M. Escudero-Escribano, E.A. Paoli, R. Frydendal, T.W. Hansen, I. Chorkendorff, I.E. Stephens, J. Rossmeisl, Enabling direct H₂O₂ production through rational electrocatalyst design, *Nat. Mater.* 12 (2013) 1137–1143.

[61] M. Melchionna, P. Fornasiero, M. Prato, The rise of hydrogen peroxide as the main product by metal-free catalysis in oxygen reductions, *Adv. Mater.* 31 (2019), e1802920.

[62] L. Chen, J. Yu, X. Zhang, P. Guan, R. Su, Theoretical modeling of site selectivity and chemical substitution effect of H₂O₂ production efficiency on modified graphene, *Catal. Lett.* 151 (2021) 390–397.